The application of apertured filter method to the simultaneous measurement of particle-turbulence interaction in dilute suspension layer under oscillatory sheet flows

C. Liu[1,*], K. Kiger[2]

1: Dept. of Mechanical engineering, University of Maryland, College Park, USA
2: Dept. of Mechanical engineering, University of Maryland, College Park, USA
*Corresponding author: cliu1213@umd.edu

Keywords: Multi-phase measurement, PIV imaging technique, Phase discrimination, Sediment transport, Sheet flow, Particle-turbulence interaction

ABSTRACT

One of the challenges confronted in particle image velocimetry (PIV) measurements applied in multi-phase flows is the discrimination of signals from different phases simultaneously registered in each single monochromatic camera. In the current sheet flow study, the sediment particles with a mean diameter of $240\,\mu m$ are used and the diameter of tracer particles ranges from $25 \sim 50\,\mu m$. Under conventional imaging, the disparity in particle sizes would inevitably cause highly imbalanced reflected signals from the two phases and the image quality of one of the phases typically must be sacrificed. This manuscript introduces a low-cost and exceedingly convenient solution, named as the apertured filter method, which is characterized by the combined use of fluorescent tracer particles and an optical band pass filter with a round hole drilled in the center, with the hole diameter comparable to the smallest lens aperture size. It is demonstrated that the apertured filter method can provide balanced image intensities among the sediment and tracer particles and preserve the identifiability and separability of both phases. To compute the carrier phase velocity, median filter subtraction (Kiger & Pan, 2000) is applied to the acquired images, followed by direct implementation of stereoscopic PIV (SPIV) process. The cross-talk PIV errors due to the presence of sediment particles are assessed and found to be within $0.3\,pixels$ up to a sediment concentration of $C = 1\%$. Enabled by the apertured filter method and the multi-camera single-plane (MCSP) method developed by Liu & Kiger (2022), a whole field, phase-locked time-resolved, particle-resolved and concurrent measurement of both the fluid and the sediment phase within the dilute regime ($C \leq 1\%$) in a sinusoidal oscillatory sheet flow (period, $T = 5\,s$, and peak free stream velocity, $U_{o,p} = 1\,m/s$) is achieved. Such detailed measurements in sheet flow have never been reported before to the author's best knowledge. The analysis of the acquired data focused upon three phase angles when the external flow is reversing the direction. The phase averaged sediment concentration, mean velocities for each phase and slip velocities between the two phases are evaluated.

1. Introduction

In a coastal environment, sand particles on the seafloor can be mobilized by the bottom boundary shear flow generated by surface waves and currents, which can result in various bed features, such as vortex ripples in low-flow regime, or a flat bed under sheet flow conditions. Sheet flow is characterized by its intensive sediment transport rate and the existence of a thick layer of suspended sediment particles. Even under well controlled laboratory flow conditions, where sediment is typically modeled as well-sorted mono-dispersed particles and simplified bottom boundary layer flow is prescribed (such as fully developed or repeatable oscillatory flow), it is still proved to be very challenging to accurately model the sediment transport process. The difficulty originates from the strongly coupled particle-turbulence interaction and inter-particle interaction that is exhibited in this flow regime due to the wide range of volumetric concentrations varying from $C \approx 60\%$ (random close packing) to $C \sim O(10^{-5})$ across the boundary layer. Due to the rapid increase in the computational power, numerical simulations have been extensively used to resolve the sediment transport dynamics at different scales, however, they either involve closure models whose formulations are subject to debate or require computational costs that are not affordable in the foreseeable future. Further improvement and validation on these numerical models require detailed experimental measurements with sufficient spatial and temporal resolutions to help ascertain how the coupling is locally manifested. From this perspective, a whole-field, time-resolved, particle-resolved and concurrent measurement of both the carrier phase and sediment particles would be ideal. Past sheet flow studies consist of abundant measurements under well-controlled laboratory conditions and in field studies, however, they typically focus on measurements of the sediment kinematics and concentration and are missing the concurrent coupled details between the fluid and the particles.

In the current work, an experimental investigation of sediment transport mechanisms under sinusoidal oscillatory sheet flow conditions is conducted, with an emphasis in the dilute regime ($C \leq 0.01$), where significant fluid turbulence is present, strong particle-turbulence interaction occurs and inter-particle collisions can be neglected. A PIV/PTV-based multi-camera measurement is implemented to provide a whole-field, phase-locked, time-resolved, particle resolved and concurrent measurement of both the fluid and the sediment phase within the dilute regime. These measurements are achieved through the use of a thin laser light sheet with a nominal thickness of $1 \sim 2\,mm$ to constrain our focus in narrow regions and allow measurements of more concentrated particles (Liu & Kiger, 2022). The experimental details are presented in Sec. 2. For the sediment phase, only the particles located close to the light sheet center are 3D reconstructed and Lagrangian particle tracking (LPT) is applied to compute sediment trajectories; while for the continuous carrier phase measurement, stereoscopic PIV is used due to its superior reliability. A novel measurement technique, named the apertured filter method, is developed to facilitate the separation of signals reflected by the two phases and enable the concurrent measurement up to a concentration of $C \leq 0.01$, which will be elaborated in Sec. 3. With this method, multi-camera and time-resolved measurements at every 10° within each sheet flow cycle has been conducted. Preliminary results of the kinematics during flow reversal for both phases are discussed in Sec. 4. Conclusions are provided in Sec. 5.

2. Experimental details

Oscillatory sheet flow is generated in the UMD U-tube water tunnel, whose schematic is presented in Fig. 1, with its dimensions, the coordinate system used hereafter and the measurement location and area indicated. The bottom 15 cm is packed with well-sorted sand particles, with the particle properties shown in Table 1. The piston in the tank on one end is used to drive the oscillatory flow in the horizontal test section. The piston motion is precisely controlled by a feedback control system equipped with a position sensor directly monitoring the instantaneous piston position. The resultant free stream velocity in the test section varies with time as, $U_o(t) = U_{o,p}\sin(2\pi t/T), m/s$, where $U_{o,p} = 1\,m/s$ is the nominal magnitude of the free stream velocity and $T = 5\,s$ is the bulk flow oscillation period. The associated flow properties are summarized in Table 2. The detailed laser and camera configurations are presented in Fig. 2, in which a Nd:YLF laser (Photonics Industries, DM60-527) and three high-speed cameras (Phantom v640/641, Vision Research, 4-megapixel, 12 bit depth) each equipped with a $105\,mm$ lens (Nikon Micro NIKKOR, $f_{\#} = 5.6$) and an apertured optical filter (SHOTT OG550 $2\,mm$ thick, $3\,mm$ in dia. hole) are used. The resultant camera spatial resolution is $26 \sim 28\,\mu m/pixel$ for all the cameras (this number varies across the field of view due to the oblique viewing angles of each camera). Multiple spherical and cylindrical lenses are used to converge the laser beam overcoming a long travel distance ($\sim 6\,m$) after which it is spread into a sheet of light at the measurement location with a nominal thickness of $1 \sim 2\,mm$. Fluorescent tracer particles of diameters ranging from $25 \sim 50\,mum$ are used for carrier phase measurement. Custom made viewing prisms were placed between the cameras and the test section to alleviate the astigmatism effect caused by the inclined viewing angles of the cameras. The cameras and the prisms were both mounted on an aluminum frame, which was bolted directly to the steady concrete floor. A soft connection is created between the prism frame and the test section side wall using heavy-duty plastic film, creating a volume that was filled with water. In this way, any flexure or vibrations in the test section caused by the flow when running experiments can be effectively isolated from the imaging system.

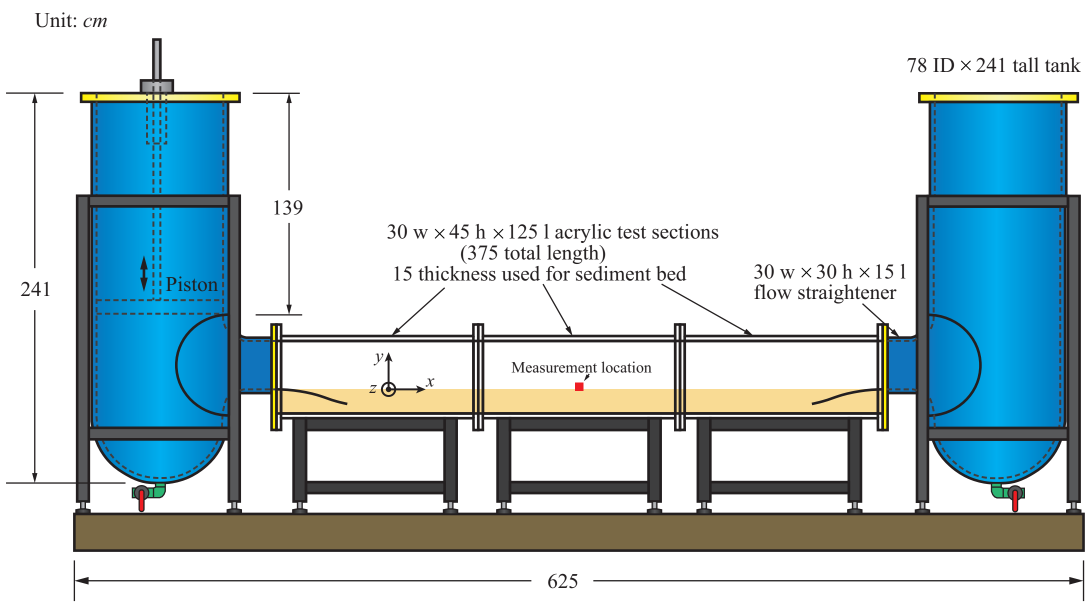

Figure 1. The U-shaped oscillatory flow tunnel.

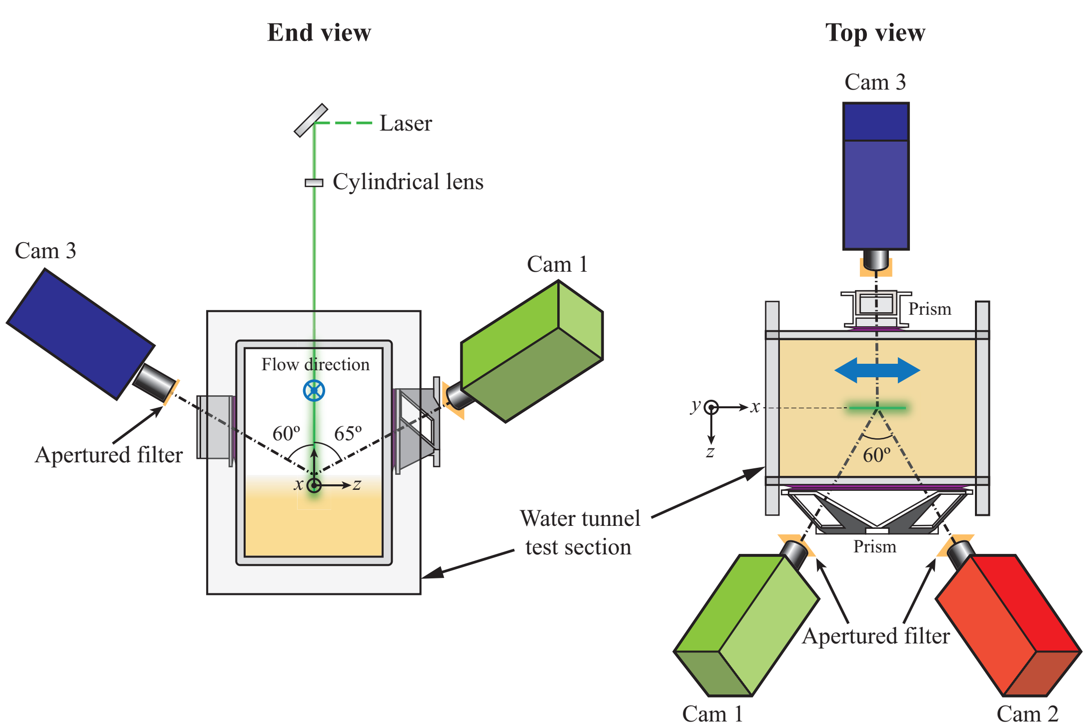

Figure 2. The laser and camera configurations.

In order to conduct phase-locked measurements at every 10° within each sheet flow cycle ($T = 5\ s$), a precise triggering scheme is required to synchronize the motion of the piston with the imaging system. This is realized by a laser-photodetector triggering system, which consists of a photodetector secured with the piston and a static Helium-Neon laser precisely aligned with the photodetector when the piston is initially at the mid-stroke position. Pulse signals are generated by the photodetector every time the piston returns to the mid-stroke position and are used as a reference for the phase-locked imaging. The uncertainty in phase synchronization achieved under current triggering scheme is estimated to be below $\pm 10\,ms$, equivalent to $\pm 0.72^{\circ}$ in phase, or ± 20 images in each time resolved measurement (75 consecutive frames at an imaging frequency of $2000\,Hz$).

Table 1. Fluid and sediment particle parameters

Fluid density, ρ_f	$998\,kg \cdot m^{-3}$
Fluid kinematic viscosity, ν	$9.6 \times 10^{-7}\,m^2 \cdot s^{-1}$
Particle mean diameter, d	$240\,\mu m$
Particle density, ρ_p	$2500\,kg \cdot m^{-3}$
Specific gravity, $s = \rho_s/\rho_f$	2.5
Particle settling velocity, W_s	$3.06\,cm/s$
Particle response time, τ_p	$5.64\,ms$
Particle Reynolds number, $Re_p = u_{\tau,p} d/\nu$	17.0
Wall Stokes number, $St_w = \tau_p u_{\tau,p}^2/\nu$	27.1

Table 2. Flow condition parameters

External flow oscillation period, T	$5\,s$
External flow peak velocity, $U_{o,p}$	$1\,m/s$
External flow peak acceleration, $a_{o,p}$	$1.26\,m/s^2$
Semi-excursion length, l_{se}	$0.80\,m$
Bulk Reynolds number, $Re = U_{o,p}H/\nu$	$300,000$
Shields parameter, θ	1.31
Fall parameter, R_p	14.85
Sleath parameter, S	0.085
Bottom shear stress, $\tau_{b,p}$	$4.61\,Pa$
Bottom friction velocity, $u_{\tau,p} = \sqrt{\tau_{b,p}/\rho_f}$	$6.80\,cm/s$

3. Measurement technique development

In the current study, concurrent PTV/PIV measurement of both the sediment particles and the carrier phase flow are conducted in sheet flow conditions to gain a better understanding of the coupled dynamical behavior of the two phases. The multi-camera single-plane (MCSP) PIV method has been developed for a reliable 3D reconstruction of sediment particles (up to an optical depth of order $O(1)$) within a well-defined thin measurement volume near the light sheet center (Liu & Kiger, 2022). Once the instantaneous sediment particle distribution is acquired, the sediment phase concentration can be easily computed by counting the particles number within some suitably prescribed measurement volume. Given a time-resolved measurement, sediment particle trajectories and the associated particle-resolved dynamics can be computed by Lagrangian particle tracking (LPT). This manuscript, on the other hand, will focus on presenting a novel measurement technique that is capable of reliably extracting the carrier phase velocities with the presence of sediment particles up to a volume fraction of $C \sim 1\%$ without sacrificing the sediment measurement. In this section, an overview of the past work on how the tracer images were extracted and carrier phase velocities were subsequently computed in multiphase flow measurements is first provided, followed by the challenges confronted when applying the existing phase separation techniques directly in the current sheet flow measurements. This motivates a novel imaging method using fluorescent tracer particles along with an apertured long pass filter, which is demonstrated to achieve decent images qualities and preserve excellent identifiabilities of both phases.

3.1. Past literatures on phase discrimination

In multiphase flow measurement, researchers have proceeded in two ways to separate the signals from each phase, one is based upon optical discrimination according to the difference in the emission wavelengths of each phase and the other one is via image post-processing. Optically separating the signals from each phase normally requires the use of fluorescent tracer particles and band-pass filters in front of multiple cameras selectively registering the signals from only one of the phases (Poelma et al., 2006; Blois et al., 2015; Elhimer et al., 2017); or the use of RGB cameras (Hagiwara et al., 2002); or the use of dual illuminating sources (Lindken & Merzkirch, 2002; Kim et al., 2022). In sheet flow measurement, the conventional combined use of fluorescent tracer particles with optical long pass filer can effectively remove the unwanted signals of the sediment particles to enable the direct measurement of the carrier phase, however additional cameras without optical filters must be added to resolve the sediment phase if concurrent measurement is required. Past studies (Poelma et al., 2006; Blois et al., 2015; Elhimer et al., 2017) typically employed this method only for planar PIV measurement, in which a total of two cameras (one for each phase) are adequate. However, when applying this method in a volumetric measurement imaging configuration, which often requires at least three cameras for each phase, a concurrent two-phase measurement would consist of a total of six cameras, which is not only unaffordable for most labs but also can be very space-consuming and potentially causes difficulties in the arrangement of these cameras near the experimental facilities. Thus it is highly favorable to register both phases in a single monochromatic camera and then use image post-processing techniques to separate each phase. This motivates the novel apertured filter method, which aims to optimize the image quality of both phases registered in each single camera and achieve comparable measurement capability and accuracy that could only be previously achieved by assigning cameras dedicated to the measurement of each phase separately.

With both phases captured in a single monochromatic camera, the phases can be discriminated by various image processing techniques developed in the previous studies, either according to the difference in the particle image characteristics (Kiger & Pan, 2000; Khalitov & Longmire, 2002); using digital masking technique (Gui et al., 1997; Lindken & Merzkirch, 2000; Song et al., 1999); distinguishing characteristic features in the correlation plane/vector post-processing stage (Delnoij et al., 1999; Deen et al., 2002; Seol & Socolofsky, 2008); or by machine learning (Ilonen et al., 2018; Poletaev et al., 2020; Xue & Katz, 2019).

3.2. Limitations with conventional imaging

The difficulty with carrier phase measurement originates from the huge disparities in the image intensities of the sediment particles and the tracer particles (due to their size difference) and the much higher target sediment concentration. The state-of-the-art phase separation technique, the median filter subtraction (MFS, Kiger & Pan (2000)) method, is used to first filter out the sediment signals, followed by application of a standard stereoscopic PIV process to the presumably tracer-dominated images. This method proves to be accurate under very dilute concentrations, typically less than $C \sim O(10^{-4})$. In the current study, however, the concentration is several orders of magnitude higher, which significantly degrades the method's performance. As shown in Fig. 3 (upper half of the fourth row first column plot), when the sediment concentration reaches $C \approx 0.1\%$, significant sediment residuals remain even after MFS is applied, having the same or even higher intensity level than the tracer particles. These residual signals apparently dominate the image intensity in most interrogation regions ($32 \times 32\, pixel^2$) and will bias the cross-correlation peak and generate errors in carrier phase measurement. When the sediment concentration further increases to $C \approx 1\%$, only very few tracer particles are visible in the raw image as shown in Fig. 3 (lower half of the second row first column plot). Most tracers, even if not physically blocked by the surrounding sediment particles, blend into the high background noise created by the relatively strong scattered light from the sediment particles residing outside of the light sheet.

In order to reduce the signals from the dispersed phase particles, optical filtering is commonly used (Poelma et al., 2006; Blois et al., 2015; Elhimer et al., 2017). In the current study, sediment particles directly reflect the laser light, which has a narrow wavelength spectrum peaked at 527 nm. When fluorescent tracer particles (Rhodamine WT, diameter $25 \sim 50\, \mu m$, peak emission wave length $590\, nm$) are used, combined with long pass optical filters (SCHOTT OG550, cut-on wavelength $550\, nm$) applied in front of cameras, significantly enhanced tracer signals can be achieved comparing to the sediment signals as shown in Fig. 3 (the second row third column plot). However, the degradation of the image contrast of sediment particles is so severe that many of the particles become indistinguishable and can no longer be identified with the current phase detection algorithm (Khalitov & Longmire, 2002). This naturally motives the idea of creating a small opening at the center of the applied long pass filter to transmit additional scattered light of all wavelengths through the filter, with the primary purpose to enhance the sediment signals in the wavelength of the laser that are normally blocked by the filter. We name the proposed solution as the "apertured filter method". A photo of the fabricated apertured filter consistently used in the current study is shown in Fig. 3 (the first row second column plot), in which the center hole is cut by a waterjet cutting machine (Omax ProtoMAX).

3.3. Description of Apertured Filter method

The working principle of the apertured filter method is straightforward and can be easily explained assuming an ideal optical long pass filter, which has 100% rejection and transmission rate for the laser light and the fluorescence light respectively. Without the center hole, only the fluorescent tracer particles can be registered in the cameras; by inducing a small opening (much smaller than the camera aperture size), the image intensities of fluorescent tracer particles are still primarily governed by the camera aperture size and thus remain almost the same, whereas the sediment particle intensities are solely determined by the hole size on the filter and should be proportional to the hole area. In effect, with only one single camera, the two phases can be simultaneously imaged under two different "camera aperture" settings independently, i.e. the aperture used for sediment particles are fixed to the size of the hole, and the aperture used for tracer particles are determined by camera lens aperture being used. Moreover, even with a fixed hole size on the apertured filter, by simply adjusting the camera aperture ($f_{\#}$), the relative intensities of the two phases can be theoretically adjusted to a wide range of ratios to customize for specific applications. The effectiveness of apertured filter method is demonstrated in Fig. 3, where two-phase images were recorded and compared under three different camera settings, with no optical filter ($f_{\#} = 11$), with apertured filter ($f_{\#} = 5.6$) and with conventional optical filter ($f_{\#} = 5.6$). In this figure, identical distributions of both the sediment particles and the tracer particles under identical illuminations are imaged, and the only factor influencing the resultant image characteristics is the application of the different types of filters. The two-phase suspensions are generated in a gel-box with statically suspended sediment and tracer particles of prescribed volumetric fractions (Knowles & Kiger, 2012), which has a similar vertical concentration profile as that measured in an actual sheet flow. The raw images in Fig. 3 (the 2nd row plots) were extracted from a region where the sediment concentration transitions from 0.2% (upper half) to 1% (lower half). The locations of identified sediment particles (red solid circles) and the identified tracer particles (green solid squares) are marked on the raw images and the median filtered images respectively. Human interventions were used when identifying the tracer particles. The size-brightness distributions of all the identified sediment particles and tracer particles are also plotted in Fig. 3 (the 3rd row plots). It is clearly shown in the figure that there is a significant underestimation of the identifiable tracer particles and sediment particles in the "no filter" case and the "conventional filter" case respectively; while the apertured filter method can produce balanced signals and adequate image quality of both phases to permit reliable extraction of each phase independently. The bottom row of plots also show that with the apertured filter method, MFS ($3 \times 3\, pixel^2$, [4]) can produce a much cleaner filtration of sediment signals, which makes the filtered image suitable for direct stereoscopic PIV process.

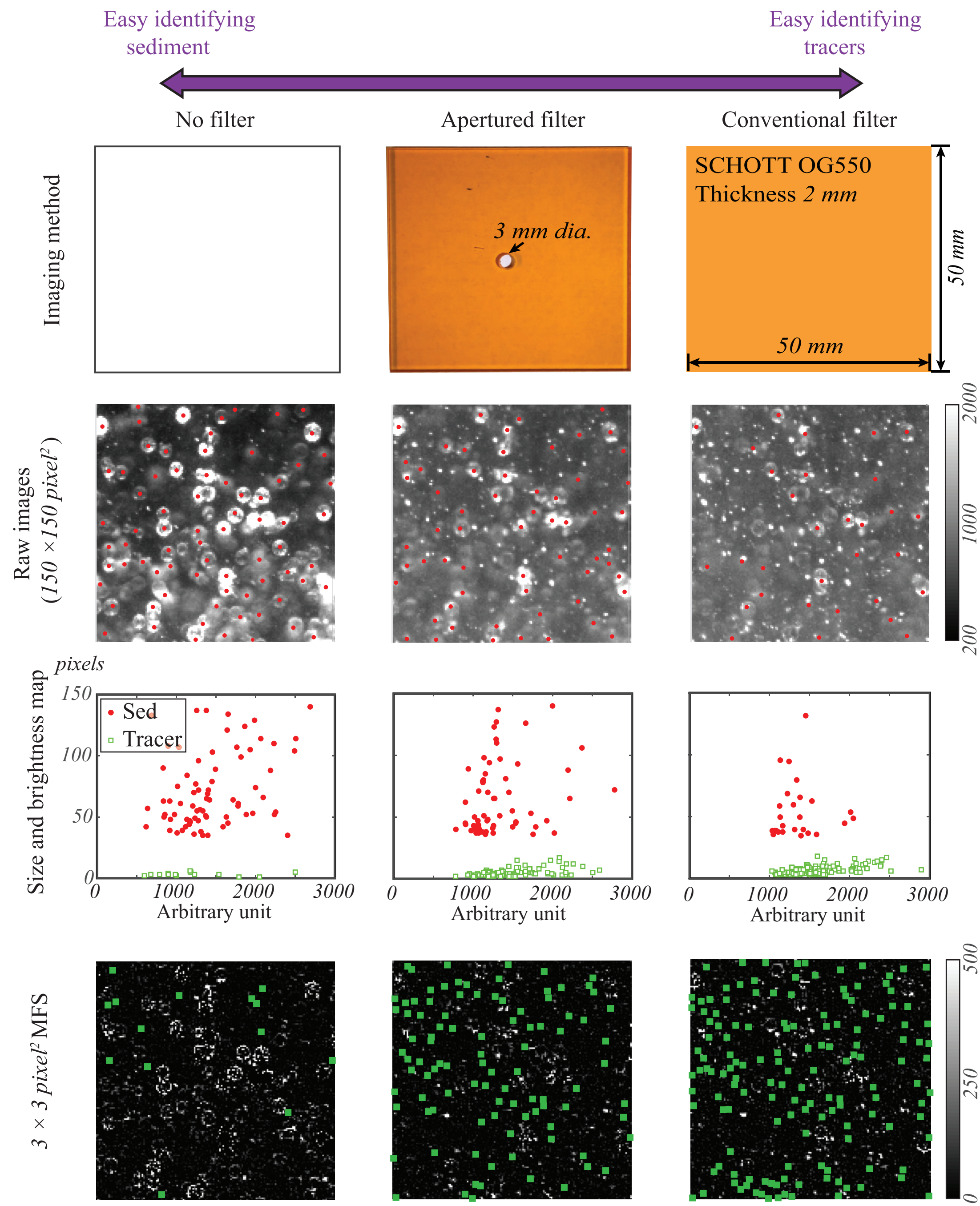

Figure 3. The recorded images of the sediment and tracer particles both statically suspended in hydrogel under three different image settings. The first row shows the 3 image settings applied (with no filter $f_{\#} = 11$, with apertured filter $f_{\#} = 5.6$ and with conventional filter $f_{\#} = 5.6$), followed below by the raw images captured under the corresponding camera settings, with identified sediment particles denoted by red solid circles. Median filter subtraction is applied to each raw image and their results are shown in the bottom row, with identified tracer particles marked as green solid squares. In the third row, size-brightness maps are generated for each sediment and tracer particle identified. The raw images were extracted from a region where the sediment concentration transitions from 0.2% (upper half) to 1% (lower half).

Several technical questions confronted when fabricating the apertured filter are addressed below to assist potential users with the same needs to customize their own apertured filter. Specifically, these are: 1) selection of commercial optical filter characteristics, 2) mechanical vignetting effects introduced by the aperture, and 3) camera focus aberrations.

For commercial filter selection, the pass band needs to have a suitable cut-on wavelength that separates the dominating wavelengths of the two phases (i.e. laser wavelength compared to the fluorescence emission band), preferably with a large rejection optical density (OD > 2) and a small slope factor. An ideal transmission curve (maximum OD in blocking and 100% transmission band, with step transition at the cutoff wavelength) can allow a larger range of adjustment of relative image intensities between phases.

The mechanical vignetting effect can cause image degradation, and occurs when mechanical components protrude into the imaging path of the camera lens, typically manifesting as darkening of image corners. For apertured filter imaging, the centrally placed symmetric hole could potentially form a brighter image center and dark areas towards the image periphery. According to lens image formation theory and several validation tests conducted, we found that the vignetting effect is sensitive to the following camera settings: the hole size on the filter (D_a), the camera aperture ($f_{\#}$), the filter-to-lens distance (l), the thickness of the filter (h) and the angular field of view (θ_{fv}, ratio of camera sensor size to lens focal length). A general rule of thumb is to keep all of the above five parameters as small as possible to prevent the vignetting effect. In the current imaging set-up, a 105 mm focal length lens (Nikon Micro NIKKOR) was used resulting in an angular field of view of $\theta_{fv} = 6.8^{\circ}$. The filter thickness and hole diameter are $h = 3mm$ and $D_a = 2\,mm$, respectively. The filter is taped directly to the front surface of the camera lens to achieve a zero filter-to-lens distance. With these parameters fixed, different camera apertures ($f_{\#}$) were tested, and it was found that with $f_{\#} \leq 11$, the vignetting effect was completely eliminated (no noticeable darkening of image corners) for our optical conditions. An empirically recommended value for the opening size on the optical filter is between the smallest and the third smallest camera lens aperture size.

The fact that the filter represents a region of inhomogeneous media implies that it can also alter the quality of the camera focus. The hole at the filter center creates a disparity of the optical paths length (OPL) for light rays emitted from the focal plane traveling through the filter versus through the hole directly onto the camera sensor. In order to alleviate the focusing problem, the thickness of the optical filter needs to be as small as possible to reduce the disparity in the OPL, unless some index-matching material is cast into the hole. This issue can also be mitigated by increasing the camera aperture $f_{\#}$, however as illustrated above, there is an upper limit in the $f_{\#}$ to avoid the vignetting effect. With the 2 mm thick apertured filter (SCHOTT glass, $n_d = 1.51$) used in the current study, focused particle images of both phases can be achieved with camera apertures of $f_{\#} \geq 4$.

The velocity measurement uncertainties for both the sediment particles and the carrier phase are quantified below. The sediment particle velocity uncertainties were estimated by investigating the particle velocity fluctuations along each trajectory. For the carrier phase, the majority of uncertainties stem from the "cross-talk" errors induced by sediment signals, so following the same method used by Khalitov & Longmire (2002) and Kiger & Pan (2000), composite two-phase images were used, in which two sets of single-phase images (carrier and sediment respectively) were acquired separately and then synthesized together to form artificial two-phase images. The sediment phase images were recorded from the static suspension of sediment particles in the hydro-polymer gel. The filtered artificial two-phase images by median filter subtraction (Kiger & Pan, 2000) along with their source single-phase tracer images were all directly fed to Davis 10 for stereoscopic PIV process. The interrogation window size is set to be $64 \times 64\, pixel^2$, roughly the same as the thickness of the light sheet, corresponding to a cubic measurement volume of $1.5 \times 1.5 \times 1.5\, mm^3$. The resultant velocity vectors computed with the source single-phase images are used as the high-fidelity reference for the artificial two-phase images to compare with. Under the highest target concentration of $C = 1\%$, the resultant mean absolute instantaneous velocity errors in the in-plane directions are $0.5\, cm/s$ in carrier phase and $0.6\, cm/s$ for sediment particles and the out-of-plane errors are about 1.5 times of the corresponding in-plane ones.

4. Results and discussion

Although phase-locked time-resolved measurements were conducted for full stroke cycles, the measured kinematics can be equivalently mapped to phases within the first half of a cycle through a straightforward coordinate transformation due to flow temporal symmetry. As shown in Figure 4, the free stream velocity during the first half-cycle accelerates from zero in the positive $x-$direction until reaching the maximum nominal velocity of $1\, m/s$, and then decelerates back to zero. Only the results at three phases are reported in this manuscript, which corresponds to the three moments near flow reversal as shown in the shaded region: 1) $170°$, just before the external flow ceases, 2) $0°$, right when the bulk flow is momentarily at rest and 3) $10°$, shortly after the flow direction reverses. The time evolution of statistics should be compared in the sequence of $170° \to 0° \to 10°$, which will be consistently associated with a different color in all of the figures presented in this section (red $\to$ green $\to$ blue).

The coordinate system consistently used when reporting the measured quantities is shown in Figure 4, in which $x-$ is the streamwise direction, $y-$ is the normal-to-bed direction and $z-$ is the spanwise direction. $z = 0\, mm$ corresponds to the light sheet center, which is in the middle of the test section; and $y = 0\, mm$ corresponds to the static bed height before experiment starts. The homogeneity of flow in both $x-$ and $z-$ directions were validated in the work of Knowles (2009). The instantaneous velocities decomposed in the $x-$, $y-$ and $z-$ directions are denoted as U, V and W respectively, with subscript "f" referring to flow properties and "p" the sediment particle properties. An overbar, "–", is used to indicate phase averaged quantities, which is defined as:

$$\overline{\Psi_f}(y|\varphi) = \frac{1}{N}\sum_{i=1}^{N}\frac{1}{\Delta x \Delta t}\int\int \Psi_{f,i}(x,y,t|\varphi)dxdt \tag{1}$$

for an instantaneous flow variable under field representation, $\Psi_f(x,y,t)$. In the above equation, $\varphi = 0° \sim 170°$ indicates the phase angle being averaged, $\Psi_{f,i}$ denotes the flow field quantity acquired at the i th realization from an ensemble of $N = 84$ independent realizations, $\Delta t = 37.5\, ms$ is the time duration of each time-resolved measurement at each phase, and $\Delta x = 31\,mm$ is the overall width of the measurement region. To compute the average of a sediment variable, $\Psi_p(x_p, y_p, t)$, which exists only at discrete points identified as a sediment particle, a binning method is used to search and average all the identified particles contained within each horizontal bin $y - \Delta y/2 \leq y_p < y + \Delta y/2$. The vertical phase averaged profile of a quantity associated with sediment phase can be written as,

$$\overline{\Psi_p}(y|\varphi) = \frac{1}{N_p} \sum_{i=1}^{N} \sum_{j=1}^{N_{\Delta t}} \sum_{k=1}^{N_{ij}(y)} \Psi_{p,ijk}(y|\varphi) \tag{2}$$

where $N_{\Delta t} = 75$ is the total number of time-resolved images (total time steps) acquired at each phase per realization, $N_{ij}(y)$ represents the number of particles found within the bin located at height y, at the j th time step and in the i th realization, and $N_p = \sum_{i=1}^{N} \sum_{j=1}^{N_{\Delta t}} \sum_{k=1}^{N_{ij}(y)} 1$. The binning height, Δy, increases from 1 to $2\,mm$ with the elevation (y) to contain enough particles in each bin for converged statistics ($N_p > 1000$ for all bins and $N_p > 10,000$ in most bins). Since each individual sediment particle directly interacts with its local ambient flow, the statistics of a fluid quantity that are sampled only at particle's instantaneous locations (x_p, y_p) should also be studied. We refer to such a quantity as "particle-conditioned" and its instantaneous representation is denoted as $\Psi_f|_p(x_p, y_p, t)$ or $\Psi_f|_p$, whose statistics will be shown later to provide insight into the coupled dynamics of the particle and fluid motions. Its value is computed by interpolating the fluid quantity $\Psi_f(x, y, t)$, which is available on a regular Cartesian grid in the current work, to each desired particle location (x_p, y_p). The interpolated fluid quantity represents a volume-averaged one in the neighborhood of a particle and the volume of averaging depends on the interrogation window size used in the stereoscopic PIV process, which is set to be roughly the same as the light sheet thickness, resulting in a cube with sides that are six particle diameters in length. The phase average of a particle-conditioned fluid quantity, denoted as $\overline{\Psi_f|_p}$, can be defined in the same way as shown in Eq. (2). The fluctuating component of an instantaneous quantity (Ψ_f or Ψ_p) is denoted by the corresponding lower case letter and can be expressed as $\psi = \Psi - \overline{\Psi}$. For a particle-conditioned fluid quantity, the fluctuating component is defined as $\psi_{f|p} = \Psi_f|_p - \overline{\Psi_f}$. The variance or root mean square of the fluctuating component is denoted by $\psi^{'}$. Higher order statistics can be computed in the same way as expressed in Eq. (1∼2).

4.1. Sediment concentration

Figure 5 shows the vertical profiles of the phase-averaged volumetric concentration in the dilute region ($C < 1\%$ and $y > 2\,mm$) at the three phases ($170°$, $0°$ and $10°$) near flow reversal. A log-log scale is used in the plot such that any power law relations exhibited in the concentration distribution ($C = y^{\alpha}$) are manifested as straight lines and the slope represents this power, α. The concentration profiles are qualitatively the same among these three phases. In the upper dilute region, $y > 11\,mm$, the concentration decreases with height from the bed in a power law fashion;

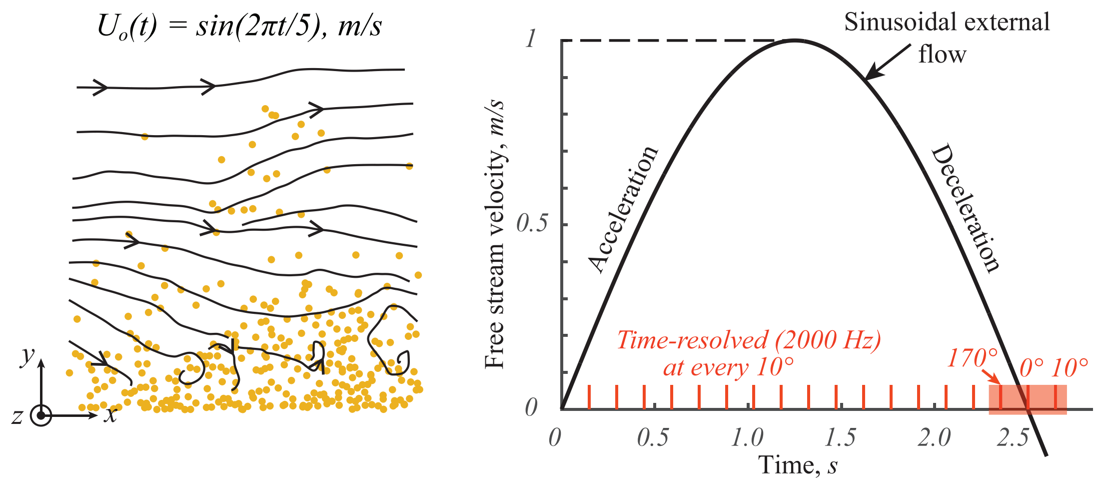

Figure 4. The flow configurations.

then in the middle dilute region, $4\,mm < y < 11\,mm$, the curve rolls off to a steeper slope; and in the narrow lower dilute region, $2\,mm < y < 4\,mm$, the power law relation seems to be recovered with a noticeably smaller magnitude exponent. A decrease of concentration is observed from phase 170° to 10° at every elevation within the height demonstrated in the figure, indicating a net transport of sediment particles towards the bed (deposition) during flow reversal. Straight lines are fitted to the concentration profiles, shown as the dashed lines in the figure, both in the upper region ($y > 11\,mm$) and in the lower region ($2\,mm < y < 4\,mm$) and their associated powers (α) are computed. From phase 170° to 10°, in the upper region ($y > 11\,mm$), the absolute value of the power, $|\alpha|$, decreases from 3.47 to 2.46 indicating that the change of concentration with height becomes milder (tending toward a more uniform distribution) as the flow is reversing; on the contrast, the fitted $|\alpha|$ in the lower region ($2\,mm < y < 4\,mm$) is increased as one goes from 170° to 10° ($|\alpha| = 0.37 \rightarrow 1.0$, indicative of strengthening stratification of the sediment in this region). The reversed changes in $|\alpha|$ over the three reversal phases in the upper and lower regions implies different sediment particle suspension mechanisms in these two regions.

4.2. Mean velocities

Figure 6 demonstrates the phase-averaged velocity profiles (decomposed in $x-$, $y-$ and $z-$ directions) of the sediment particles (solid dots symbols) and the carrier phase (solid lines) at the three reversal phases, 170°, 0° and 10°. In the streamwise direction (left plot), the carrier phase velocity profiles show the same features as those reported in a typical oscillatory turbulent boundary layer flow with non-mobile walls (Jonsson & Carlsen, 1976). The flow near the bed reverses direction before the external flow does in response to the adverse pressure gradient slowing the flow, indicating that the near bed flow leads in phase. In the outer region, the flow velocity should closely match the oscillatory velocities prescribed at the corresponding phases, i.e. $U_{o,\varphi} = U_{o,p}\sin(\varphi)\,m/s$, where $\varphi = 170^{\circ}, 0^{\circ}$ or 10°, however, the upper region of the mean profiles ($y = 33\,mm$) shows a distinct offset from $0\,m/s$ expected for $\varphi = 0^{\circ}$, as well as for phases 170° and 10°. This is consistent

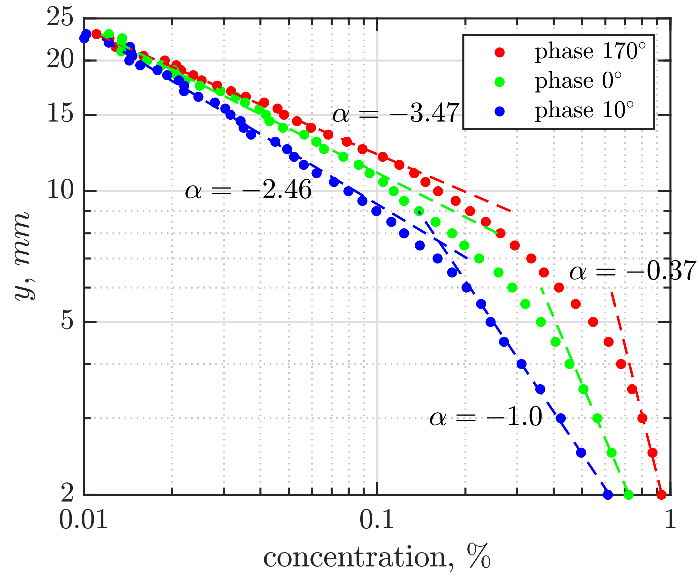

Figure 5. The mean concentration profiles at the three phases near flow reversal, at $170°$, $0°$ and $10°$.

with the boundary layer extending beyond the current measurement region and resulting from the characteristic “overshoot" commonly observed in oscillatory boundary layer flows. If measurements were made in higher elevations, it is expected that these profiles will converge back to the corresponding prescribed velocities ($U_{o,\varphi}$). A small thus detectable difference in the streamwise mean velocity between the sediment particles and the carrier phase is shown in the figure. With such small relative velocity differences, the streamwise velocities of the two phases are speculated to be roughly in phase with each other at an all elevations. More quantitative and conclusive discussions on the phase shift should use the complete set of the acquired data at every $10°$ and will not be included in this manuscript.

The normal-to-bed ($\overline{V_f}$) and spanwise ($\overline{W_f}$) phase-averaged carrier phase velocity profiles are shown in the middle and right plot of Figure 6. The fact that they are close to zero (within the uncertainty limits) provides convincing evidence on the homogeneity achieved in the flow in the spanwise and streamwise directions. The spanwise homogeneity can be directly inferred from the near-zero mean spanwise velocities observed for both the sediment particles and the carrier phase at every elevation and at all three phases angles ($\overline{W_f}$ and $\overline{W_p}$). The streamwise homogeneity can be validated by evaluating the averaged continuity equations satisfied by the carrier phase within the measurement region, which is written as below,

$$\frac{\partial \overline{U_f}}{\partial x} + \frac{\partial \overline{V_f}}{\partial y} + \frac{\partial \overline{W_f}}{\partial z} = 0 \tag{3}$$

where the Boussinesq approximation is used to neglect the effect of sediment concentration on the compressibility of the carrier phase flow, which is only valid for sufficiently low concentrations ($C < 1\%$) and is a common practice used in sediment transport models with dilute suspensions (Cantero et al., 2008). It should be noted that this doesn't justify the neglect of concentration terms

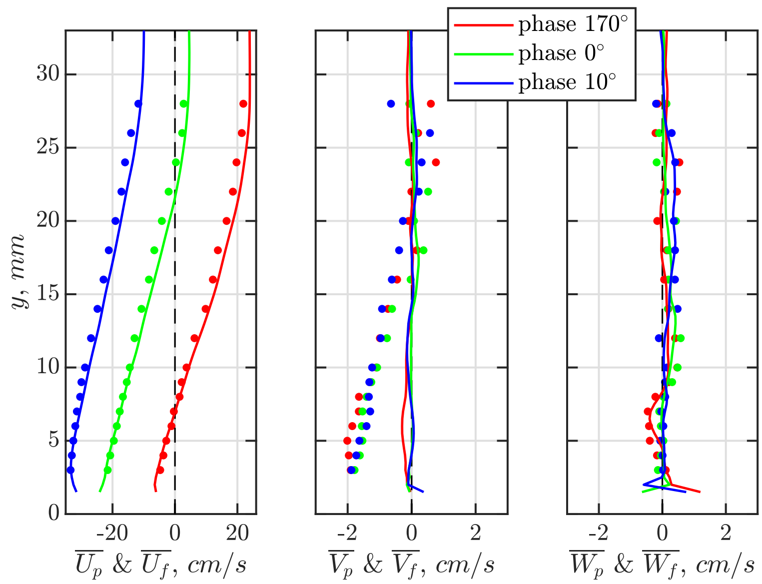

Figure 6. The mean velocity profiles of the sediment particles (dot symbols) and the carrier phase (solid lines) near flow reversal, at 170°, 0° and 10°.

in the mass equations for the sediment phase or in the momentum equations for both phases. The homogeneity of the streamwise carrier phase velocity in the streamwise direction (i.e. $\partial\overline{U_f}/\partial x \approx 0$) can be easily confirmed as a result of the last two terms being negligibly small due to $\overline{V_f}(y,t) \approx 0$ and spanwise homogeneity.

The sediment vertical (normal-to-bed) velocity profile ($\overline{V_p}$) shows an interesting behavior: for $y > 18\,mm$, there is a negligible mean vertical velocity observed for all three phase angles; while for $y < 18\,mm$, the vertical sediment velocity profiles for all three phase angles show a distinct downward velocity that increases approaching the bed. There is not a noticeable trend in the evolution of these profiles from $\varphi = 170°$ to $\varphi = 0°$, which implies that the turbulent fluctuations, which are responsible for particle suspension, are not likely to evolve much through these three phase angles.

4.3. Slip velocities

Two types of particle conditioned velocity difference are defined, $\overline{U_f|_p} - \overline{U_p}$ and $\overline{U_f|_p} - \overline{U_f}$, both of which were commonly used to reveal different aspects of particle-related flow properties (Kiger & Pan, 2002; Berk & Coletti, 2020). The former one, referred to as "particle conditioned slip velocity" following Kiger & Pan (2002) represents the statistics characterizing the instantaneous local flow seen by each sediment particle. In contrast, $\overline{U_f|_p} - \overline{U_f}$ acts as an indicator of whether the sediment particles are oversampled in certain fluid regions with faster/slower velocities in comparison to the fluid mean and will be referred to as "oversampling fluid velocity bias". If the particles were randomly located, then the conditional average of fluid velocity, $\overline{U_f|_p}$, should show no difference from the unconditioned one, $\overline{U_f}$. The two types of particle conditioned velocity differences are decomposed in three directions ($x-$, $y-$ and $z-$) and plotted in Figure 7. It is here noted in advance that there is no detectable differences in these vertical profiles among the three phase angles presented, so the following discussion will focus on the features in common to all three.

In the streamwise direction, a small ($\sim 0.4\,cm/s$), uniform and consistently negative particle conditioned slip velocities ($\overline{U_f|_p} - \overline{U_p}$) can be found at all elevations within the measurement region, as shown in the left plot of Figure 7. This implies that the sediment particles closely follow the phase-averaged temporal variations in the flow in the streamwise direction. The exceedingly small horizontal particle-conditioned slip velocity has been verified by various experimental works both in oscillatory sheet flows (Dick & Sleath, 1991) and in steady turbulent channel flows (Kiger & Pan, 2002). Contrary results were found in the work of Berk & Coletti (2020), who studied steady turbulent boundary layer flows with air-solid phases and found this term (under similar particle Stokes number, St_p, and particle Reynolds number, Re_p) is only negligibly small in outer regions and sharply increases as approaching to the wall and dominates over the "oversampling fluid velocity bias" term ($\overline{U_f|_p} - \overline{U_f}$) in the near wall region. This discrepancy is most likely due to their much larger particle-to-fluid density ratio. For the oversampling fluid velocity bias term ($\overline{U_f|_p} - \overline{U_f}$), negative values that grow away from the bed are observed, which indicates that the particles favor low-speed (or more negative) regions and that this oversampling is stronger away from the bed. Qualitatively similar behavior were also reported in both works of Kiger & Pan (2002) and Berk & Coletti (2020). In Figure 7, it is shown that for $y > 10\,mm$, a more or less constant value of $\overline{U_f|_p} - \overline{U_f}$ is observed, equivalent to approximately 30% of the bottom friction velocity ($u_{\tau,p}$ in Table 2), which is also within the same order of magnitudes as reported by Kiger & Pan (2002) and Berk & Coletti (2020). It should be noted that in the present work, the mean flow has already reversed the direction at certain elevations (see Figure 6), so the consistently negative values of $\overline{U_f|_p} - \overline{U_f}$ term, could also mean a preferential sampling of high-speed flow regions in the reversed direction, as is the case for $y > 10\,mm$ at phase $10°$ and $10 < y < 20\,mm$ at phase $0°$.

In the normal-to-bed direction, as shown in the middle plot of Figure 7, the particle-conditioned slip velocity ($\overline{V_f|_p} - \overline{V_p}$) shows constant values throughout the measurement range, which is around $2\,cm/s$ accounting for about 65% of the particle settling velocity (W_s). This means that each sediment particle statistically experiences an upward moving flow with a velocity of $2\,cm/s$, which provides drag forces and is responsible for the suspension of sediment particles. The fact that the measured particle-conditioned slip velocity is smaller than the still-fluid particle settling velocity is also observed in the work of Kiger & Pan (2002). Preferential sampling of fluid velocities at particle locations also exists with the normal-to-bed velocity component, demonstrated by the profiles of the term $\overline{V_f|_p} - \overline{V_f}$. It is shown that the sediment particles favor to locate in the upward moving regions in the flow, with stronger oversampling away from the bed. The variation of $\overline{U_f|_p} - \overline{U_f}$ and $\overline{V_f|_p} - \overline{V_f}$ with height seems to show a consistent pattern, by combining these two profiles, it can be inferred that for the particles away from the bed, they tend to appear in flow regions where ejection of slow moving fluid ("ejection events") occurs and this preferential sampling decays near the bed. This agrees with findings by Kiger & Pan (2002) and Berk & Coletti (2020), in both of which quadrant analysis was conducted to confirm the ejection events. In the spanwise direction, the particles seem to be able to closely follow the ambient flow and don't show a preferential residence in terms

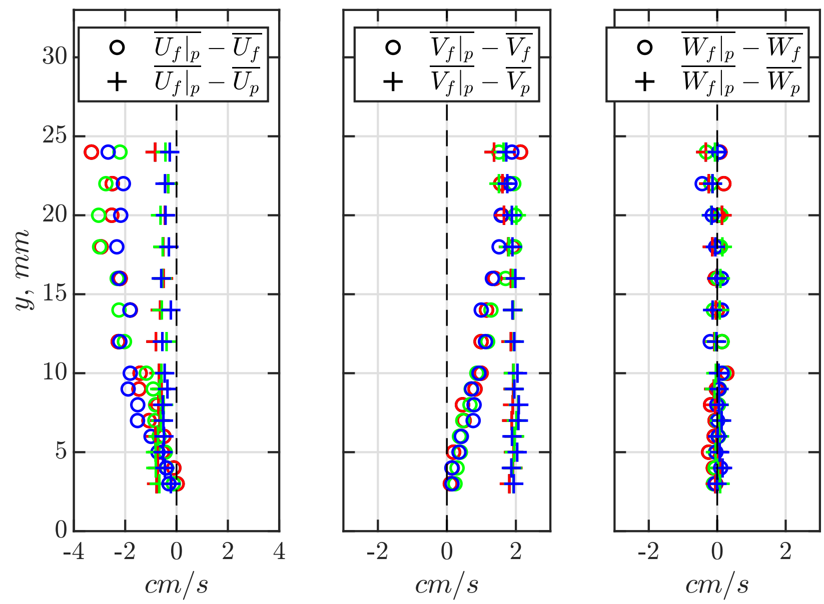

Figure 7. The particle-conditioned slip velocity profiles (+) and the oversampling of fluid regions faster/slower than the mean (∘), decomposed in streamwise (left), normal-to-bed (middle) and spanwise (right) directions at the three reversal phases, 170° (red), 0° (green) and 10° (blue).

of the spanwise velocity.

Quadrant analysis was performed to provide further evidence on the oversampling of sediment particles at locations with ejection events ($u_f < 0$ and $v_f > 0$) in the flow, as shown in Figure 8 at phase 0°. Qualitatively similar behavior can be observed at the other two phase angles. Figure 8 (a), (c) and (e) illustrate the joint probability density functions of the streamwise and normal-to-bed velocity fluctuations for particle-conditioned fluid (red lines), which is superimposed on the unconditioned fluid results (black lines) for comparison. The comparison is conducted at three different elevations from the static bed, corresponding to three distinct values of $\overline{U_f|_p} - \overline{U_f}$ and $\overline{V_f|_p} - \overline{V_f}$ observed in Figure 7. The inclined and elongated shape of these contour lines (especially for $y = 10\,mm$ and $y = 22\,mm$) indicates the prevalence of flow events contributing to the negative Reynolds shear stress. It is also observed that as y increases, the contours of the particle-conditioned fluid velocity distribution demonstrates an increased shift towards the second quadrant (Q2, ejection events) direction away from the unconditioned one. At $y = 4\,mm$, the contour lines almost overlap with each other indicating a very weak preferential sampling of particle residence near the bed; whereas further away from the bed ($y = 10\,mm$ and $y = 22\,mm$), the shifted contour lines highlights the tendency of sediment particles to over-sample events in the second quadrant Q2 ($u_f < 0$ and $v_f > 0$) and under-sample those in the fourth quadrant Q4 ($u_f > 0$ and $v_f < 0$, referred to as sweeps). Figure 8 (b), (d) and (f) computes the percentage of flow events belonging to each of the four quadrants as shown in (a), (c) and (e) respectively, for the particle-conditioned (red lines) and unconditioned fluid (black lines). This again shows an increased preferential sampling of ejection events (Q2) over sweeps (Q4) at larger distance from

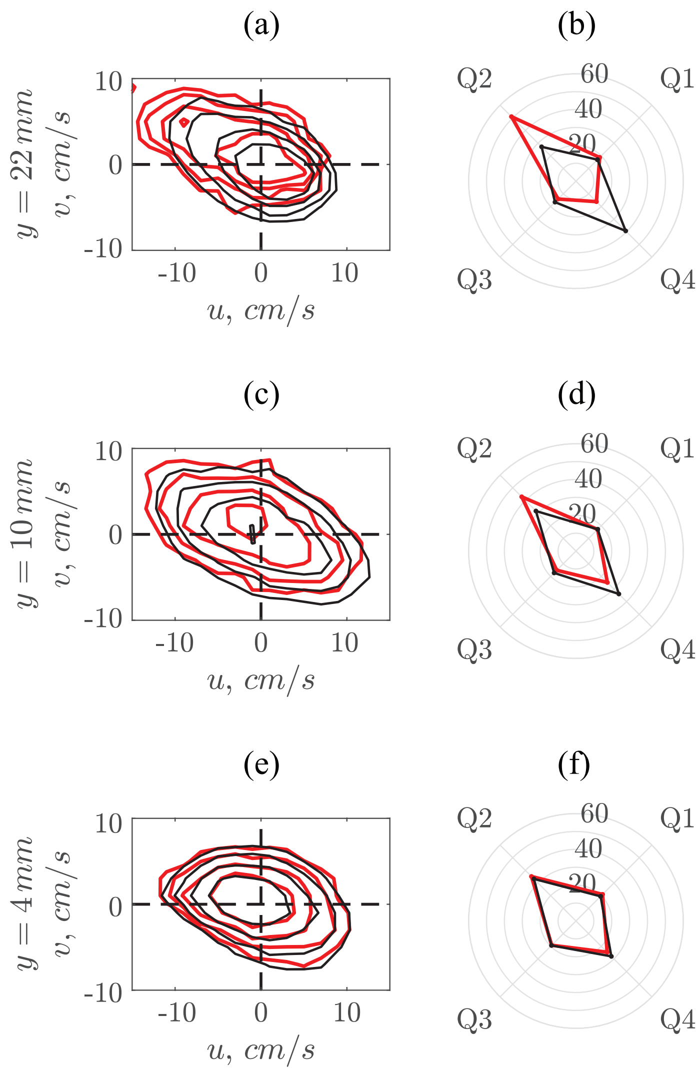

Figure 8. At phase $0°$, joint probability density functions of streamwise and vertical velocity fluctuations for the fluid (black lines) and particle-conditioned fluid (red lines), at three different elevations, (a) $y = 22\,mm$, (c) $y = 10\,mm$ and (e) $y = 4\,mm$, with contours at levels of 0.001, 0.002, 0.004 and 0.007. (b), (d) and (f) shows the percentage of undondtioned (black lines) and particle-conditioned (red lines) fluid events in each quadrant at the same three elevations.

the bed. The particles don't seem to show a significantly biased sampling in the first and third quadrant at the three elevations shown in the figure.

5. Conclusions

In this manuscript, a whole field, phase-locked time-resolved, particle-resolved and concurrent measurement of both the fluid and the sediment phase within the dilute regime ($C \leq 1\%$) in a sinusoidal oscillatory sheet flow ($U_{o,p} = 1\,m/s$, and $T = 5\,s$) has been conducted. The measurement was realized by the application of two novel PIV imaging techniques that are recently developed: 1) the apertured filter method introduced in this manuscript, used to optimized the image quality of both phases registered in each single monochromatic camera, and 2) the multi-camera single-plane (MCSP) method developed by Liu & Kiger (2022), used to facilitate the 3D reconstruction of sediment particles near the light sheet center. The apertured filter method is characterized by the use of fluorescent tracer particles in conjunction with conventional band-pass optical filter with a round hole (with a diameter comparable to the smallest the camera lens aperture) drilled at the center. It is demonstrated that this method was able to produce adequate image quality of both phases allowing for a reliable extraction of each phase independently. Some guidance on the fabrication of the apertured filter are addressed to assist potential users.

For the sediment phase measurement, concentration was computed by counting the number of particles within a well-defined measurement volume and Lagrangian particle tracking (LPT) was implemented to compute sediment trajectories over successive frames and the associated kinematics. For the carrier phase measurement, stereoscopic PIV (SPIV) process was directly implemented after the sediment signals were filtered from the acquired two-phase images by median filter subtraction (MFS, Kiger & Pan (2000)). The resultant spatial resolution (constrained by the local light sheet thickness) for the SPIV measurement is about six times of the particle diameter or twice of average inter-particle distance under the highest concentration of our interest ($C = 1\%$, corresponding to an average inter-particle distance of $\lambda_p = 3.7\,d$). The PIV cross-talk errors were evaluated and less than $0.3\,pixels$ of mean absolute displacement errors were achieved under the highest concentration of our interest ($C = 1\%$).

In this manuscript, the coupled dynamics between the sediment and carrier phase was analyzed at the three phase angles ($170°$, $0°$ and $10°$), during which the external flow is reversing the direction and experiencing a maximum adverse pressure gradient. Some important findings are summarized below:

1) In the phase-averaged concentration profiles, power law relations are observed in both the upper dilute regime ($y > 11\,mm$) and the lower dilute regime ($2 < y < 4\,mm$) with decreased exponent magnitude approaching the bed. A reversed change in the exponent over the three phase angles is found in these two regions. This is indicative of different sediment particle suspension mechanisms occurred in these two regions.

2) In the phase-averaged streamwise velocity profiles, the velocity difference between the sediment and the fluid is within 8% of the maximum velocity for all three phase angles; for $y < 18\,mm$, the sediment vertical velocity profile show a distinct downward velocity that increases approaching the bed for all three phase angles, which indicates a net settling of sediment particles towards the bed during flow reversal.

3) The particle conditioned slip velocity shows negligible values in the streamwise direction ($\overline{U_f|_p} - \overline{U_p} \approx 0$) and an almost constant value throughout the measurement height in the normal-to-bed direction ($\overline{V_f|_p} - \overline{V_p} \approx 2\,cm/s = 65\% \times W_s$).

4) Strong preferential sampling of sediment particles in flow regions with ejection events (Q2) is found for $y > 11\,mm$, while the over-sampling diminishes towards the bed.

References

Berk, T., & Coletti, F. (2020). Transport of inertial particles in high-reynolds-number turbulent boundary layers. *Journal of Fluid Mechanics*, *903*.

Blois, G., Barros, J. M., & Christensen, K. T. (2015). A microscopic particle image velocimetry method for studying the dynamics of immiscible liquid–liquid interactions in a porous micro-model. *Microfluidics and Nanofluidics*, *18*(5-6), 1391–1406.

Cantero, M. I., Balachandar, S., & Garcia, M. H. (2008). An eulerian–eulerian model for gravity currents driven by inertial particles. *International Journal of Multiphase Flow*, *34*(5), 484–501.

Deen, N. G., Westerweel, J., & Delnoij, E. (2002). Two-phase piv in bubbly flows: Status and trends. *Chemical engineering & technology*, *25*(1), 97–101.

Delnoij, E., Westerweel, J., Deen, N., Kuipers, J., & van Swaaij, W. (1999). Ensemble correlation piv applied to bubble plumes rising in a bubble column. *Chemical Engineering Science*, *54*(21), 5159 - 5171. doi:

Dick, J., & Sleath, J. F. (1991). Velocities and concentrations in oscillatory flow over beds of sediment. *Journal of Fluid Mechanics*, *233*, 165–196.

Elhimer, M., Praud, O., Marchal, M., Cazin, S., & Bazile, R. (2017). Simultaneous piv/ptv velocimetry technique in a turbulent particle-laden flow. *Journal of Visualization*, *20*(2), 289–304.

Gui, L., Lindken, R., & Merzkirch, W. (1997). Phase-separated piv measurements of the flow around systems of bubbles rising in water. In *Asme fedsm* (Vol. 97, pp. 22–26).

Hagiwara, Y., Murata, T., Tanaka, M., & Fukawa, T. (2002). Turbulence modification by the clusters of settling particles in turbulent water flow in a horizontal duct. *Powder technology*, *125*(2-3), 158–167.

Ilonen, J., Juránek, R., Eerola, T., Lensu, L., Dubská, M., Zemčík, P., & Kälviäinen, H. (2018). Comparison of bubble detectors and size distribution estimators. *Pattern Recognition Letters*, *101*, 60–66.

Jonsson, I. G., & Carlsen, N. A. (1976). Experimental and theoretical investigations in an oscillatory turbulent boundary layer. *Journal of Hydraulic Research*, *14*(1), 45–60.

Khalitov, D. A., & Longmire, E. K. (2002, Feb 01). Simultaneous two-phase piv by two-parameter phase discrimination. *Experiments in Fluids*, *32*(2), 252–268. doi:

Kiger, K., & Pan, C. (2000). Piv technique for the simultaneous measurement of dilute two-phase flows. *Journal of fluids engineering*, *122*(4), 811–818.

Kiger, K., & Pan, C. (2002). Suspension and turbulence modification effects of solid particulates on a horizontal turbulent channel flow. *Journal of Turbulence*, *3*(1), 019.

Kim, D., Schanz, D., Novara, M., Seo, H., Kim, Y., Schröder, A., & Kim, K. C. (2022). Experimental study of turbulent bubbly jet. part 1. simultaneous measurement of three-dimensional velocity fields of bubbles and water. *Journal of Fluid Mechanics*, *941*.

Knowles, P. L. (2009). *Sediment suspension events from ripple beds in oscillatory flow: Experiments* (Unpublished doctoral dissertation). University of Maryland, College Park.

Knowles, P. L., & Kiger, K. T. (2012, Mar 01). Quantification of dispersed phase concentration using light sheet imaging methods. *Experiments in Fluids*, *52*(3), 697–708. doi:

Lindken, R., & Merzkirch, W. (2000). Velocity measurements of liquid and gaseous phase for a system of bubbles rising in water. *Experiments in fluids*, *29*(1), S194–S201.

Lindken, R., & Merzkirch, W. (2002). A novel piv technique for measurements in multiphase flows and its application to two-phase bubbly flows. *Experiments in fluids*, *33*(6), 814–825.

Liu, C., & Kiger, K. T. (2022). Multi-camera single-plane piv imaging in two-phase flow for improved dispersed-phase concentration. *Experiments in Fluids*, *63*(2), 1–15.

Poelma, C., Westerweel, J., & Ooms, G. (2006, Mar 01). Turbulence statistics from optical whole-field measurements in particle-laden turbulence. *Experiments in Fluids*, *40*(3), 347–363. doi:

Poletaev, I., Tokarev, M. P., & Pervunin, K. S. (2020). Bubble patterns recognition using neural networks: Application to the analysis of a two-phase bubbly jet. *International Journal of Multiphase Flow*, *126*, 103194.

Schanz, D., Gesemann, S., & Schröder, A. (2016, Apr 27). Shake-the-box: Lagrangian particle tracking at high particle image densities. *Experiments in Fluids*, *57*(5), 70. doi:

Seol, D.-G., & Socolofsky, S. A. (2008, Aug 01). Vector post-processing algorithm for phase discrimination of two-phase piv. *Experiments in Fluids*, *45*(2), 223–239. doi:

Song, X., Shen, L., Murai, Y., & Yamamoto, F. (1999). Separation of particle-bubble images in multiphase flow. In *International workshop on piv'99- santa barbara, 3 rd, santa barbara, ca* (pp. 15–20).

Xue, X., & Katz, J. (2019). Formation of compound droplets during fragmentation of turbulent buoyant oil jet in water. *Journal of Fluid Mechanics*, *878*, 98–112.